

Linear correlation between active and resistive stresses informs on force generation and stress transmission in adherent cells

Hélène Delanoë-Ayari,^{1,*} Nicolas Bouchonville,² Marie Courçon,³ and Alice Nicolas^{2,†}

¹*Univ. Claude Bernard Lyon1, CNRS, Institut Lumière Matière, 69622 Villeurbanne, France*

²*Univ. Grenoble Alps, CNRS, LTM, 38000 Grenoble, France*

³*Univ. Grenoble Alps, CEA, Inserm, BIG-BGE, 38000 Grenoble, France*

(Dated: June 8, 2022)

Animal cells are active, contractile objects. While bioassays address the molecular characterization of cell contractility, the mechanical characterization of the active forces in cells remains challenging. Here by confronting theoretical analysis, finite element modeling and experiments, we analyze the relevance of existing mechanical approaches and show that their complementarity allows us to characterize both the resistive and the active components of the intracellular stresses that build up following cell adhesion. By highlighting their linear correlation, we show that these mechanical approaches allow us to localize the stress generators in the cells, give an upper bound to their size, and demonstrate that they are mechanically linked to the substrate at a very local scale.

Keywords: biological physics, mechanobiology, traction force microscopy, intracellular stress microscopy, elasticity

Animal cells have contractile capabilities that make cells tensed objects. This contractility allows for instance adherent cells to probe the mechanical properties of their environment and adapt to them [1–3]. Dysfunction of cell contractility is a hallmark of many pathologies, such as cancers, cardiac or brain pathologies [4, 5]. As it is strictly regulated and adapts to external physical or chemical perturbations [6], the analysis of cell contractility often brings information on the interplay of specific signaling pathways with the extracellular environment. For example, stem cell differentiation was shown to be closely regulated by the level of contractility of the tissue they are part of [7]. When asking about cell contractility, the biological question is in general to identify, locate and quantify the biochemical processes in cells that give rise to cellular forces, contractile or tensile stresses. The activity of molecular motors for instance results in mechanical stresses [2, 8]. Changes in the conformation of these proteins generate molecular movements that mechanically translate into generation of forces at the molecular level. In cell biology, these sources of stress are sought using molecular markers thus setting assumptions on the biological nature of the intracellular stress generators.

More recently, a need for label-free approaches to assess cell contractility has emerged. Their objective is to identify the areas of stress generation and to quantify their amplitude. Optical methods have been proposed that measure the density of cytoskeleton fibers in the absence of staining [9]. With even less assumption on the origin of stress generation, mechanical approaches have been implemented that quantify intracellular mechanical stresses [6, 7, 10, 11]. These methods are based on the measurement of the deformation of the extracellular environment the cells are adhering to and exploit it to calculate cell internal stresses. Here we focus on these mechanical approaches. We make explicit the origin of the stress each of these methods calculate,

which indeed differ. By confronting theoretical, numerical and experimental analysis, we show that these mechanical approaches bring a consistent picture of cell intracellular stresses in adherent cells. As a main result, we show that taking into account all these approaches allows to locate stress generators and quantify the active and resistive components of the intracellular stresses induced by cell adhesion. This analysis also brings a new picture of the interaction of the cells with the substrate, showing the existence of mechanical links between the stress generators and the substrate.

The original idea of the mechanical approaches is to model cells as materials subjected to internal volume forces, the active molecular forces mentioned above. When the cells are adhered to a substrate, the internal forces are transmitted to the substrate and deform it. Following Ref. [10], these methods infer the intracellular stresses from the deformation of substrate. Assuming that cell colonies as well as single cells can be modeled as a thin plate, the mechanical equilibrium writes (Fig. 7):

$$\vec{f}_{act} + \vec{f}_c - \vec{f}_m = \vec{0} \quad (1)$$

with \vec{f}_{act} the active cellular forces that cells build up following adhesion, \vec{f}_c and $-\vec{f}_m$ respectively the reaction force of the cell body and the resistance of the deformable substrate opposed to these active forces, all modeled as surface forces because of the thin plate approximation. \vec{f}_m is precisely the traction stress field measured by traction force microscopy (TFM) [14]. In the present work, our aim is to characterize \vec{f}_{act} and \vec{f}_c .

Eq. (1) can be reformulated in terms of the stress tensors S_{act} and S_c :

$$h \operatorname{div} S_{act} + h \operatorname{div} S_c - \vec{f}_m = \vec{0} \quad (2)$$

with h is the thickness of the plate model. S_{act} is the stress tensor that is derived from the internal cellular

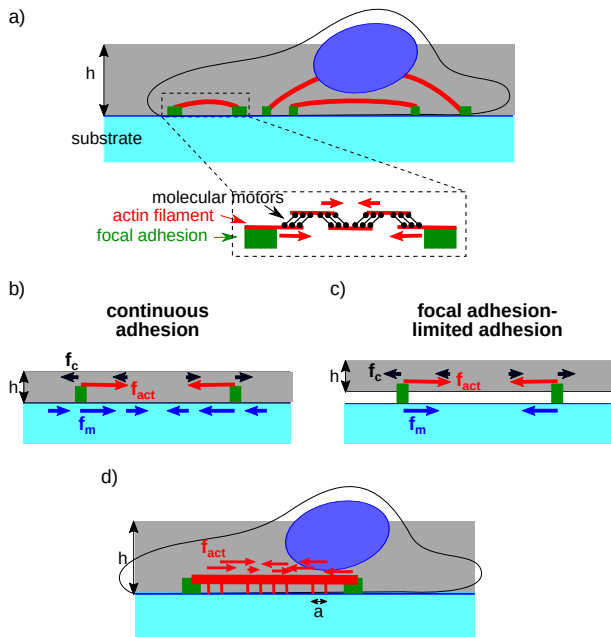


FIG. 1. Modeling of an adherent cell for intracellular stress calculation. a) Schematic of an adherent cell. Actin filament (in red) are attached to focal adhesions which are composed of adhesion proteins (in green). Molecular motors make actin filaments slide respective to each other when changing conformation. As a result the cell body gets tensed. h is the mean height of the cell. The cell is modeled as a thin plate with thickness h . b) A first assumption is to assume that intracellular stresses are transmitted to the extracellular environment through large contact areas, e.g. all over the cell area. Active intracellular forces, \vec{f}_{act} , give rise to a resistance $-\vec{f}_m$ from the substrate that spreads out of the points where active stresses are generated. The cell body opposes a resistance \vec{f}_c . c) A second possibility is that the cell only stresses the extracellular environment at the focal adhesions. The resistance of the substrate is concentrated at the adhesion points. d) Our results show that the stress generators (e.g. the acto-myosin stress fibers) are connected to the substrate with discrete anchorages of size smaller than the experimental sampling size a , and transmit locally their stress to the substrate.

force generation following cell adhesion. This stress can be addressed by a thought experiment: in the absence of adhesion, a cell that bears the same level of active stress would contract till a size determined by the balance with the reactive stress S_0 the cell body opposes to its contraction. S_{act} is then the stress that an operator must bring to restore the correct size of the cell when adhering it to the substrate. It is therefore the opposite of the reactive stress S_0 that the cell material opposes to the active forces in the absence of substrate resistance. Finally, S_c is the stress that results from the strain of the adhered cell material in response to the internal forces \vec{f}_{act} . Both S_{act} and S_c measure stresses in cells following cell adhesion. Prestresses preceding cell adhesion are not accessible here.

Eq. (2) assumes that the cells or the cellular colonies can be modeled as a thin plate, meaning that the deformation field is fairly uniform in the thickness of the cellular material. From an experimental point of view, this assumption is valid as soon as the cellular material has a much larger width than height, which is generally the case even for single cells, and when the rigidity of the substrate is comparable or lower than the rigidity of the cellular material (otherwise, in-depth shear stresses become dominant [15]).

The original method, the Monolayer Stress Microscopy (MSM) [10, 11], addresses the resolution of Eq. (1) by building a stress tensor S_{tot} that gathers both unknown S_{act} and S_c into a single stress tensor S_{tot} :

$$S_{tot} = S_{act} + S_c \quad (3)$$

$$h \text{div} S_{tot} = \vec{f}_m \quad (4)$$

Eq. (4) is underdetermined [16]. An additional relationship between the stress components is added by assuming that the cellular material has a linear elastic rheology [11, 17]. In line with MSM, Bayesian Inference Stress Microscopy (BISM) was proposed [7]. It also solves the equilibrium Eq. (4) but accounts for the noise in \vec{f}_m and does not assume a rheological model a priori for the cell material. Underdetermination of Eq. (4) is resolved by using Bayesian inversion and assuming that S_{tot} has a gaussian distribution. BISM then introduces a regularization step that allows limiting the contribution of noise in the calculated stress tensor. The rheological properties can be inferred a posteriori, by comparing the temporal derivatives of the elastic strain tensor and the spatial gradient of the velocity field in the cell material [7].

Differently, Intracellular Stress Microscopy (ISM) addresses the quantification of the resistive component of the intracellular stress, S_c , that opposes the contraction of the adhered cell [6]. When the cell is modeled as a thin elastic plate, it is straightly obtained by differentiating the displacement field of the neutral plane of the plate [13]. This approach can be extended to visco-elastic rheology when the cell material behaves like a Maxwell fluid [19], a rheological behavior that was for instance reported in flowing epithelial monolayers [20]. When the basal surface of the cell material is uniformly adhered to the substrate, either by integrin-mediated adhesions, non specific adhesions or other types of adhesive machinery such as lectins (see [21] and below for a discussion relative to this assumption), the displacement field of the neutral plane of the plate is identical to the displacement field on the top of the substrate. The resistive stress then

writes:

$$S_c = \begin{pmatrix} \sigma_{xx} & \sigma_{xy} \\ \sigma_{xy} & \sigma_{yy} \end{pmatrix}$$

$$\text{with } \begin{cases} \sigma_{xx} = \frac{E_c}{1-\nu_c^2} \left(\frac{\partial u_x}{\partial x} + \nu_c \frac{\partial u_y}{\partial y} \right) \\ \sigma_{yy} = \frac{E_c}{1-\nu_c^2} \left(\frac{\partial u_y}{\partial y} + \nu_c \frac{\partial u_x}{\partial x} \right) \\ \sigma_{xy} = \frac{E_c}{2(1+\nu_c)} \left(\frac{\partial u_x}{\partial y} + \frac{\partial u_y}{\partial x} \right) \end{cases} \quad (5)$$

(x, y) are the in-plane coordinates, E_c and ν_c are the Young's modulus and the Poisson's ratio of the cell material of thickness h , and $u_{x,y}$ are the in-plane components of the displacement field on top of the substrate. The displacement field is measured as in TFM, by the use of fluorescent markers embedded in the substrate. As a consequence of Eq. (13), implementation of ISM requires to know the Young's modulus of the cell E_c and its Poisson's ratio ν_c but is independent of the thickness of the contractile plate, h .

MSM or BISM and ISM thus do not address the same intracellular stresses. MSM or BISM calculates the bidimensional total stress tensor $hS_{tot} = h(S_{act} + S_c)$ (Eq. (4)) while ISM quantifies the Young's modulus-normalized resistive stress tensor S_c/E_c (Eq. (13)). For cell biology issues, a quantity of prime interest is \vec{f}_{act} , the internal cellular surface forces at the origin of cell contractility. In principle, combination of MSM or BISM and ISM will provide hS_{act} (Eq. (3)) from which \vec{f}_{act} can be derived. This nevertheless requires that (i) the assumption of continuous cell adhesion that bases ISM is valid, and (ii) that the 2D Young's modulus of the contractile plate, hE_c , is known (as well as the Poisson's ratio ν_c).

To go further, we first checked the validity of the calculation of S_c and S_{tot} with ISM and BISM respectively, using Finite Element Modeling (FEM). BISM was preferred to MSM as experimentally, TFM can only provide \vec{f}_m with a non negligible noise level of more (and often much more) than 10% [12]. To this end, the cell material was modeled as an elastic plate uniformly bound to the substrate (Fig. 2a). Effect of contractile and tensile force dipoles was analyzed. S_{ISM} compared well with S_c in consistence with the plaque assumption (Fig. 2c). S_{tot} was calculated as the difference between the resistive stress tensors of the adhered plate (S_c) and of the non adhered plate ($S_0 = -S_{act}$). It was compared to BISM calculation whose value of the regularization parameter was chosen based on the noise level of \vec{f}_m (see SI-1). BISM did reconstruct S_{tot} by using appropriate boundary conditions (Fig. 2d and SI-2).

We then investigated the intracellular stresses in rat embryonic fibroblast cell line REF52 (Fig. 3). The REF52 cell line we used was stably transfected with fluorescent paxillin (gift from A. Bershadsky), so to compare the location of intracellular stresses and focal adhesions. The geometry of the single cells was consistent with the

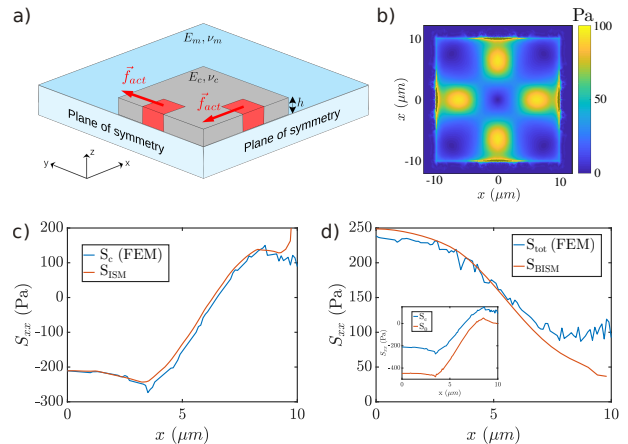


FIG. 2. FEM calculation of intracellular stresses in an elastic plate ($E_c = 5kPa$, $\nu_c = 0.5$, $h = 1\mu m$) bound to a deformable substrate ($E_m = 1kPa$, $\nu_m = 0.5$). a) Schematics of the numerical experiment. The plate is submitted to contractile and tensile force dipoles respectively along the x and y axis with truncated gaussian profile (amplitude $1kPa/\mu m$, standard deviation $2\mu m$) concentrated in $5\mu m$ wide squared dots. b) Amplitude of the surface stresses \vec{f}_m on the substrate. c) Comparison of the intracellular resistive stress S_c calculated with FEM and ISM calculation S_{ISM} (Eq. (13)). d) Comparison of the total intracellular stress $S_{tot} = S_c - S_0$ and BISM calculation S_{BISM} (Eq. (4), regularization parameter $L = 0.003$). The inset shows the profiles of $S_0 = -S_{act}$ and S_c used in the calculation of S_{tot} .

plaque approximation, the height of the cells being at a maximum of $5\mu m$ (data not shown) to be compared to their in-plane extent of order of 50 to 100 μm . Single cells were grown on a soft polyacrylamide hydrogel of 3 kPa functionalized with fibronectin. The hydrogel was loaded with a high density of 200nm fluorescent markers. The deformation field of the substrate was quantified by comparing images of beads located close to its top surface in the presence of cells and when the cells are removed. Beads displacements were measured using a pyramidal optical flow algorithm (SI-1). The surface forces \vec{f}_m were calculated using Fast Fourier transformation of the displacement field [5]. We first observed that the traction stress field did not evidence correlations with the distribution of the focal adhesions (Fig. 3b). This suggests that cell intracellular stresses are transmitted to the extracellular matrix also out of focal adhesions (Fig. S9). Since the calculation of S_c by ISM only makes sense when the cell body is firmly bound to the substrate, we limited stress calculation to paxillin-positive regions and to regions where \vec{f}_m is above the noise level (Fig. 3c). In these regions, the fact that the cell-to-matrix stress field \vec{f}_m is out of the noise implies that the cell is adhered and intracellular stresses are transmitted to the substrate. S_{tot} was calculated in the same regions using BISM algorithm,

the parameter of regularization being chosen as for the FEM calculation (Fig. 3d). Comparison of BISM and ISM revealed a linear correlation between both, with a negative slope (Fig. 3e). In addition, following a previous work where we had reported on a linear relationship between the amplitudes of $divS_c$ and \vec{f}_m [21], we confirmed this linear correlation for this other cell type. Components of the divergence of the resistive stress tensor S_c correlate with surface force components \vec{f}_m with a minus sign (Fig. 3f):

$$div \frac{S_c}{E_c} = -\frac{\vec{f}_m}{h_0 E_m} \quad (6)$$

with E_m the Young's modulus of the matrix and h_0 a characteristic length. As visible on Fig. 3f, positively paxillin-labeled pixels are indistinguishable from unlabeled pixels. This observation provides an additional argument for enlarging the regions of cell adhesion out of focal adhesions [21].

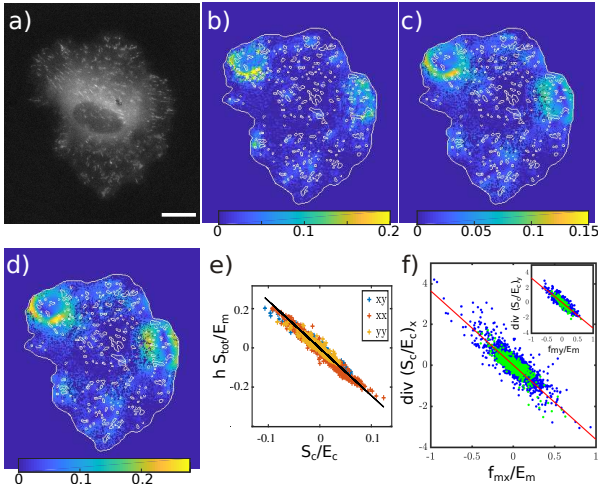


FIG. 3. a) Focal adhesions in REF52 stably transfected for YFP-paxillin. Bar $20 \mu m$. b) Amplitude of \vec{f}_m/E_m superimposed with the cell contour and the contour of the paxillin-stained adhesions (in white). Significant cell-to-matrix stresses are measured out of paxillin-stained adhesions. c) Amplitude of S_c/E_c measured at places where \vec{f}_m exceeds noise level. d) Amplitude of hS_{tot}/E_m in μm , calculated at the same places (regularization parameter $L = 0.06$). e) The components of hS_{tot}/E_m and S_c/E_c show a linear correlation (slope $2.28 \mu m^{-1}$). f) The components of $divS_c/E_c$ and \vec{f}_m/E_m are proportional (slope $2.27 \mu m^{-1}$). Green dots are for paxillin-labeled pixels, blue dots for unlabeled pixels.

To understand these linear correlations, we calculated the theoretical relationship between $divS_c$ and \vec{f}_m in a model system that consists of a thin elastic layer continuously bound to a semi infinite elastic medium and stressed by a local stress field (SI-3 and Fig. S3). As the surface forces \vec{f}_m are linked to the displacement field through a Green function [13], the relationship between

$divS_c$ and \vec{f}_m is of similar shape: a non local relationship, with a combined influence of the stresses from both in plane directions. We however obtained that this non local relationship can be approximated to a local proportionality because (i) the off-diagonal terms in the Green function are two orders of magnitude smaller than the diagonal terms (Fig. S4), and (ii) the diagonal terms are fast decaying functions close to the force point (Fig. S5). Because of this fast decay, the relationship between $divS_c$ and \vec{f}_m is sensitive to the ratio of the lateral extent of \vec{f}_m and the sampling size of the grid that is used to perform TFM or stress calculations. Actually, a linear correlation between $divS_c$ and \vec{f}_m was obtained when the lateral extent of the surface forces \vec{f}_m is smaller than the sampling size (Fig. 4a and Fig. S6(a-c)). The opposite case, where the amplitude of the surface forces spreads on a width larger than the sampling size leads to a non linear correlation, different from the experimental observation (Fig. 4(a-b) and Fig. S6(d-f)). Facing the model with the experimental observation thus leads to the conclusion that the surface forces that are transmitted to the substrate apply on areas that are smaller than the size of the sampling grid that is used in the experiment. So due to the size of the sampling, \vec{f}_m appears as point forces. The model then predicts:

$$h divS_c = \vec{f}_c \simeq -\alpha \vec{f}_m \quad (7)$$

where $\alpha = \frac{\pi h E_c (1 + \nu_m) (3 - 2\nu_m - \nu_c)}{3 a E_m (1 - \nu_c^2)}$ with a the size of the sampling grid and ν_c and ν_m the Poisson's ratios of the cell and the substrate. The direct calculation of the Green function (see SI-3) as well as FEM calculations confirmed a close to linear relationship between $divS_c$ and \vec{f}_m for \vec{f}_m profiles narrower than the sampling size (Fig 4a). For wider distributions of \vec{f}_m , the correlation showed two branches (Fig. 4b), a consequence of the oscillations of the Green function that couples both quantities (Fig. S5). From this analysis, we could conclude that the proportionality between $divS_c$ and \vec{f}_m that we observe in the experiment is indeed related to the small extent of the cell-to-matrix surface force field compared to the sampling size, and is anyhow an approximate linearity. Combined with the observation that the amplitude of \vec{f}_m is above the noise level in a large part of the cell (Fig. S9), we conclude that the surface forces \vec{f}_m are concentrated to very local areas whose size is below our in-plane resolution of $0.7 \mu m$, but are distributed almost everywhere beneath the cell, not restricted to focal adhesions.

Eq. (6) had introduced a characteristic length scale h_0 that should compare to $1/\alpha$ in Eq. (7). We artificially reduced the in-plane resolution to probe the dependency of h_0 with the sampling size a . As shown in Fig. S7, we obtained that h_0 is proportional to a , as predicted in Eq. (7) (see SI-4). This confirmed our analysis on the role of the sampling size in the relation between $divS_c$ and

\vec{f}_m . Combination of Eqs. (1) and (7) then implies that at points where $\vec{f}_m \neq \vec{0}$,

$$\vec{f}_{act} \simeq (1 + \alpha)\vec{f}_m \quad (8)$$

and Eqs. (4 and 7) lead to:

$$S_c \simeq -\alpha S_{tot} + \Phi \quad (9)$$

with Φ a zero divergence stress tensor set by the boundary conditions. Altogether these results lead to the conclusion that either the stress generators are small entities whose size is smaller than our sampling size, or they are mechanically linked to the substrate by discrete anchors whose size is smaller than our sampling size, not restricted to focal adhesions (Fig. 7d). This result is actually consistent with other studies that identified myosin or acto-myosin microfilaments as stress generators with size of few tens of nanometers, far below the present in plane resolution [24, 25]. Eq. (8) shows a linear relationship between stress generation \vec{f}_{act} and the surface forces \vec{f}_m . In principle, the local intracellular stress \vec{f}_{act} could give rise to a spread surface force field \vec{f}_m . Here, the spreading of \vec{f}_m is not experimentally noticeable, being either hidden by the lack of spatial resolution of our analysis, of $0.7\mu m$, and by the noise level. As a consequence, the measurement of the cell-to-matrix stress field \vec{f}_m namely gives information on the location of the intracellular stress generators (Fig. 7d).

In addition, Eq. (9) evidences a linear relationship between the stresses measured by ISM and by BISM, as obtained experimentally (Fig. 3e). In the experiment, the zero divergence stress tensor Φ is not apparent. This could be that the boundary conditions impose an amplitude for Φ that is buried in the noise or that its contribution is filtered by the regularization step in the calculation of hS_{tot} , that filters low frequencies (see SI-2). This second linear correlation is a direct consequence of the linear correlation between $divS_c$ and \vec{f}_m . It should be noted that linearity is optimal when the regularization parameter in BISM calculation is chosen with the discrepancy principle (see SI-1 and Fig. S10).

In the previous analysis, we focused on paxillin positive regions and on regions where $\vec{f}_m \neq \vec{0}$ as these regions are for certain adhered to the substrate in the limit of the spatial resolution of the experiment, of $0.7\mu m$. We now question if the previous conclusions can be extended to the other parts of the cell where the cell-to-matrix surface forces are not distinguishable from noise and focal adhesions are not visible (in red in Fig. S9). These regions that are larger than the sampling size could either support a very low level of force generation or the cell could be detached from the substrate. We focus on the case where the cell is not adhered (Fig. 7c). We tested how this situation would impact the correlation between $divS_{ISM}$ and \vec{f}_m . It should be noted that out of the areas where the cell is adhered, S_{ISM} differs from S_c as its

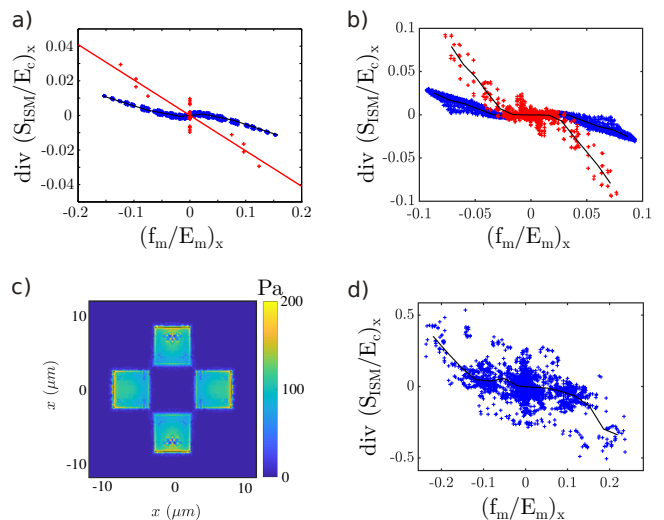


FIG. 4. Analysis of the correlation of $divS_{ISM}$ and \vec{f}_m (a-b) for a plate that is uniformly adhered to the substrate (Fig. 7b) or (c-d) for a plate with local anchorage (Fig. 7c). a) Numerical solution of Eq. (S8) for a uniformly adhered plate submitted to active forces \vec{f}_{act} with gaussian distribution as in Fig. 2. The width σ of the Gaussian field is varied relative to the size a of the sampling grid ($a = 8$ pixels, red: $\sigma = 1$ pixel; blue: $\sigma = 25$ pixels). $divS_c$ and \vec{f}_m show a linear correlation when $\sigma < a$ (goodness of the fit $r^2 = 0.83$). The dark line is a bin average of the blue points. b) FEM simulation for the same set-up. The sampling size is imposed by the mesh size and is smaller than the width of the Gaussian field (blue: force patch of $5\mu m$, standard deviation of the Gaussian field $\sigma = 2\mu m$; red: force patch of $1\mu m$, $\sigma = 0.25\mu m$). A narrower Gaussian field brings the correlation closer to a straight line. c) Amplitude map of the surface forces \vec{f}_m for a plate that is only adhered through the local patches where the active forces \vec{f}_{act} are generated (force patch of $5\mu m$, $\sigma = 2\mu m$). d) Correlation between $divS_c$ and \vec{f}_m for the locally adhered plate (same parameters as in (c)).

calculation is based on the deformation of the substrate which now differs from the deformation of the cell. Using FEM simulation, we observed that the surface forces \vec{f}_m concentrate in the regions of adhesion only (Fig. 4c). Would force generation occurs out of the adhered areas, the surface forces \vec{f}_m would change in amplitude, but the total stress hS_{tot} would not be able to show it as Eq. (4) does not contain any information on the location of the stress generators and as a consequence, the calculation of S_{tot} is less robust when the cell is not continuously adhered (Fig. S12). $divS_{ISM}$ and \vec{f}_m also showed a correlation that resembles the one obtained for adherent cells in the presence of force generators of width larger than the sampling size, but more noisy (Fig. 4d). Thus the experimental observation of a linear relationship between $divS_{ISM}$ and \vec{f}_m (Fig. 3f) may not be sufficient to conclude on the adhesive interaction of the cells with the substrate, the measure of transmitted forces \vec{f}_m that emerge from the noise being more conclusive. The in-

tracellular stresses generated in regions where the level of force transmission to the substrate is low thus remain difficult to characterize by these mechanical approaches.

In conclusion, we observe a linear correlation between the divergence of the strain tensor in the cell body and the forces that are transmitted to the substrate (Fig. 3f). This linear relation implies that independent of any assumption on the rheological properties of the cell body, the transmission of the cellular stresses to the substrate is performed through local links whose size is smaller than the sampling size of the experiment and is not restricted to focal adhesions, as depicted in Fig. 7d. When the cell has a linear elastic behavior, we show that this observation brings to the conclusion that stress generation following cell adhesion leads as a first approximation to the production of a proportional resistive stress in the cell body. It also makes it possible to localize stress generators by measuring the surface forces \vec{f}_m that cells transmit to the extracellular environment thus highlighting the sensitivity and the relevance of mechanical analysis as companion technique of biological analysis.

The authors are indebted to D. Gulino-Debrac for allowing them to use the biology lab and to P. Marcq for the provision of the BISM calculation code. This work was initiated by very fruitful discussions with E. Mazza, L. Filotto, P. Silberzan and T. Vourc'h. H. D. and A. N. are grateful to them. The authors also thank F. Graner for critical reading. A. N. and N.B acknowledge the support by ANR-12-JSVE05-0008.

- Zaman, J. P. Butler, D. A. Weitz, J. J. Fredberg, and X. Trepate, *Nat. Mater.* **10**, 469 (2011).
- [6] M. Moussus, C. der Loughian, D. Fuard, M. Courçon, D. Gulino-Debrac, H. Delanoë-Ayari, and A. Nicolas, *Soft Matter* **10**, 2414 (2014).
- [7] V. Nier, S. Jain, C. T. Lim, S. Ishihara, B. Ladoux, and P. Marcq, *Biophys. J.* **110**, 1625 (2016).
- [14] U. S. Schwarz and J. R. Soiné, *Biochim. Biophys. Acta, Mol. Cell Res.* **1853**, 3095 (2015).
- [15] A. Nicolas and S. A. Safran, *Phys. Rev. E* **69**, 051902 (2004).
- [16] S. Timoshenko and J. N. Goodier, *Theory of Elasticity*, 2nd ed. (New York-Toronto-London : McGraw-Hill Book Co., 1951).
- [17] D. T. Tambe, U. Croutelle, X. Trepate, C. Y. Park, J. H. Kim, E. Millet, J. P. Butler, and J. J. Fredberg, *PLoS One* **8**, e55172 (2013).
- [13] L. Landau and E. Lifchitz, *Theory of elasticity* (Mir Ed., 1967).
- [19] H. Delanoë-Ayari and A. Nicolas, In preparation.
- [20] S. Tlili, M. Durande, C. Gay, B. Ladoux, F. Graner, and H. Delanoë-Ayari, *Phys. Rev. Lett.* **125**, 088102 (2020).
- [21] M. Moussus, C. der Loughian, D. Fuard, M. Courçon, D. Gulino-Debrac, H. Delanoë-Ayari, and A. Nicolas, *Soft Matter* **10**, 7683 (2014).
- [12] B. Sabass, M. L. Gardel, C. M. Waterman, and U. S. Schwarz, *Biophys. J.* **94**, 207 (2008).
- [5] J. P. Butler, I. M. Tolic-Nørrelykke, B. Fabry, and J. J. Fredberg, *Am. J. Physiol. Cell Physiol.* **282**, C595 (2002).
- [24] A. Pasapera, S. Plotnikov, R. Fischer, L. Case, T. Egelhoff, and C. Waterman, *Curr. Biol.* **25**, 175 (2015).
- [25] H. Wolfenson, G. Meacci, S. Liu, M. R. Stachowiak, T. Iskratsch, S. Ghassemi, P. Roca-Cusachs, B. O'Shaughnessy, J. Hone, and M. P. Sheetz, *Nat. Cell Biol.* **18**, 33 (2016).

* helene.delanoë-ayari@univ-lyon1.fr

† alice.nicolas@cea.fr

- [1] T. R. Polte, G. S. Eichler, N. Wang, and D. E. Ingber, *Am. J. Physiol., Cell Physiol.* **286**, C518 (2004).
- [2] B. L. Doss, M. Pan, M. Gupta, G. Greci, R.-M. Mège, C. T. Lim, M. P. Sheetz, R. Voituriez, and B. Ladoux, *Proc. Natl Acad. Sci. U.S.A.* **117**, 12817 (2020).
- [3] J. Zhang, F. Alisafaei, M. Nikolić, X. A. Nou, H. Kim, V. B. Shenoy, and G. Scarcelli, *Small* **16**, 1907688 (2020).
- [4] J. M. Northcott, I. S. Dean, J. K. Mouw, and V. M. Weaver, *Front. Cell Dev. Biol.* **6**, 17 (2018).
- [5] M. Javier-Torrent and C. A. Saura, *Cells* **9**, 1926 (2020).
- [6] F. Bordeleau and C. A. Reinhart-King, *F1000Res.* **5**, 1819 (2016).
- [7] W. Ning, A. Muroyama, H. Li, and T. Lechler, *Cell Stem Cell* **28**, 1 (2020).
- [8] S. R. Peyton, C. M. Ghajar, C. B. Khatiwala, and A. J. Putnam, *Cell Biochem. Biophys.* **47**, 300 (2007).
- [9] W. Wang, J. P. Miller, S. C. Pannullo, C. A. Reinhart-King, and F. Bordeleau, *J. Biophotonics* **11**, e201800008 (2018).
- [10] N. Wang, I. M. Tolic-Nørrelykke, J. Chen, S. M. Mijailovich, J. P. Butler, J. J. Fredberg, and D. Stamenović, *Am. J. Physiol. Cell Physiol.* **282**, C606 (2002).
- [11] D. T. Tambe, C. C. Hardin, T. E. Angelini, K. Rajendran, C. Y. Park, X. Serra-Picamal, E. H. Zhou, M. H.

SUPPLEMENTARY INFORMATION

SI-1. Materials and Methods

Cell culture

Rat embryo fibroblast (REF52) lines stably expressing YFP-paxillin (gift from A. Bershadsky, Weizmann Institute of Science, Israel) were cultured in Dulbecco's modified Eagle medium (DMEM) containing 10% fetal bovine serum, 100 U/ml penicillin, 100 $\mu\text{g}/\text{ml}$ streptomycin and 100 $\mu\text{g}/\text{ml}$ glutamine. The cells were maintained at 37 °C in a humidified atmosphere of 5% CO₂. Single cell experiments were performed on polyacrylamide (PAA) hydrogels of 3 kPa loaded with dark red fluorescent beads of diameter 200 nm at concentration 2 mg/mL (ref. Mecatract from Cell&Soft®). The hydrogels were provided with a fibronectin coating of surface density of 0.8 $\mu\text{g}/\text{cm}^2$. Traction force microscopy was performed on a IX83 Olympus inverted microscope equipped with a temperature and CO₂ controlled incubation chamber (Okolab) at 60x magnification (oil immersion objective, NA 1.25).

Cellular stresses calculations

Cellular stresses were calculated from the deformation field of the fluorescent markers embedded in the PAA hydrogel. Measurements were performed 6 h post seeding. Stacks of images with 0.3 μm spacing were acquired to allow the precise determination of the surface. At the end of the experiment, cells were removed using 1x trypsin (Lonza) to get reference images of the surface of the gel in the absence of stresses.

Before calculating the displacement field, images were globally registered for global rotation and translation in x,y,z. Autocorrelation of the image of the contractile cell was performed with the reference image (*i.e.* after trypsin) at 4 different regions taken the further away possible from the cell in the corners of the image. From the displacements of these 4 areas, one could calculate the rigid registration for aligning almost perfectly the two images.

Calculation of the beads displacements due to cell forces applied on the surface was performed using a Matlab script based on the CRToolbox developed by J. Diener [1] (<https://sites.google.com/site/crtoolbox/home>), where a Kanade-Lucas-Tomasi (KLT) particle tracking algorithm [2] is used to calculate the displacement of each bead. KLT is an optical flow method, which was recently shown to be much more accurate and faster than traditional Particle Image Velocimetry Techniques (PIV) for Traction Force Microscopy [3]. This method allows tracking displacements larger than the pixel size with keeping the efficiency and the precision of optical flow algorithms. As a first step, beads positions were detected using a local maxima search algorithm imposing a minimum distance of 3 to 5 pixels in between each points. Pyramids of images (ie smaller resolution images of the initial image and of its spatial gradients of intensity) were generated following Ref. [4]. The tracking algorithm was then successively ran on the different levels of the pyramid beginning on the low resolution image. Kanade Lucas optical flow algorithm was run first on the low resolution image to get a crude estimate of the displacement field. The calculated displacements were recursively used back as initial guesses for the next pyramid levels to get a more and more accurate displacement with reduced interrogation windows around the selected features. We used a pyramid level of 4 for images of 2048 x 2048 pixels, and a value down to 20 pixels for the size of the last interrogation window. These parameters allowed us to reach a spatial resolution of 800 nm. The resolution was determined as the number of objects per unit surface that the algorithm could successfully track.

Cell-to-matrix surface forces f_m were calculated using Fast Fourier Transform, following Butler et al [5]. Resistive intracellular stress S_c were obtained from the differentiation of the in-plane displacement field [6], using a Sobel approximation of the derivative. In both cases, the sampling was chosen following Shannon criterium: in order to calculate cell-to-matrix or intracellular stresses, the displacement field was interpolated on a sampled regular grid with a frequency more than twice the maximal frequency obtained from KLT analysis. Noise level was quantified by calculating the cellular stresses out of the cell contour. Only cellular stresses that exceed the 0.95 quantile of the noise were considered to be significant.

The total intracellular stress S_{tot} was calculated following BISM method [7]. As it is quite demanding on computer memory, we used a grid of 50x50 pixels to calculate the stress, which enables a rather fast computation, so as to perform many different tests in a reasonable amount of time. Boundary conditions were enforced in the prior to correspond to the surface forces f_m at the edges of the cell (see SI-2). The hyperparameter ensuring $\sigma_{xy} = \sigma_{yx}$, was set to 10^3 as was done in [7]. The regularization parameter L was chosen according to the χ^2 estimate [8]. In BISM, this criterion expresses as $L = \ell^2 s^2 / s_0^2$, with ℓ the size of the grid sampling for the calculation of S_{tot} , s the standard

deviation of the noise of \vec{f}_m , and s_0 the standard deviation of the calculated stress hS_{tot} [7]. Since s_0 is unknown, an additional criterion is required. As detailed in Ref. [9], the choice of the optimal parameter for Eq. (4) in the main text is far from obvious. Here we follow the Morozov discrepancy principle, that states that Eq. (4) in the main text cannot be solved with a better accuracy than the noise on \vec{f}_m . So at best,

$$\|hdivS_{tot} - \vec{f}_m\| = s \quad (10)$$

We thus estimate $s_0 \simeq \ell s_1$, with s_1 the standard deviation of \vec{f}_m . Then L is simply obtained from the cell-to-matrix stress field distribution and the quantification of its noise level out of the cell boundaries: $L = s^2/s_1^2$. It is to be noted that here the L-curve criterion is not consistent with the Morozov discrepancy principle as it gives a dominant weight to the accuracy of the equilibrium equation Eq. (4) of the main text, omitting that the right hand side, \vec{f}_m is a noisy, inaccurate, data.

Finite Element Modeling

We used Comsol Multiphysics™4.2 to implement finite element modeling. The cell was modeled as a square elastic sheet of size $30 \times 30 \mu m^2$ and $1 \mu m$ in thickness with a Young Modulus $E_c = 5 kPa$ and a Poisson's ratio $\nu_c = 0.5$ (Fig 2a in the main text). This cell is sitting on the top of an elastic gel which is modeled as a parallelepiped of size $200 \times 200 \times 100 \mu m^3$ in (x, y, z) , with Young's modulus $E_m = 1 kPa$ and a Poisson's ratio $\nu_m = 0.5$. A contractile dipole is positioned along the x-axis, composed of gaussian forces of amplitude $1 kPa/\mu m$ and width σ adjusted between $(0.25$ and $2 \mu m)$. A tensile dipole is set on the y-axis with the same amplitude and width. The mesh is initialized using a normal physics control mesh. To ensure a mesh refinement just beneath the cell a mirror square is added in the gel. Finally the solver uses an adaptative mesh refinement. We take advantage of symmetries and only run the simulation on a fourth of the geometry (see Fig. 2a in the main text). The cell is adhered on the gel either through the entire cell surface or just underneath the gaussian forces on squares of size 2.5σ .

SI-2. Effect of boundary conditions and of low frequency noise in the calculation of S_{tot}

Noise strongly impacts the calculation of the force field in TFM. This problem was addressed by using a Bayesian approach [10], a regularization scheme [8] or a filtering in the Fourier space [5]. These regularization schemes were shown to filter high frequencies [11, 12]. Noise issues keep also critical in the calculation of the intracellular stresses and we question how noise impact ISM and BISM calculations. ISM is based on the derivative of the displacement field. It is therefore very sensitive to high frequency noise. A filtering is applied by the use of the Sobel approximation in the calculation of the gradients. Figure 3f in the main text shows that experimentally, the dispersions of $divS_c$ and \vec{f}_m are similar. The fact that $divS_c$ does not show many points with high amplitude out of the fit line shows that ISM is not altered by high frequency noise compared to TFM. Differently, BISM calculation is based on the integration of the cell-to-matrix surface force field. A perturbation in \vec{u} with wave vector \vec{q} results in a perturbation of the stress tensor of order of $\Delta S_{tot} \propto 1/q$. Low frequency noise thus strongly alters the value of S_{tot} . And indeed, the regularization scheme in BISM calculation damps these low frequencies (Fig. 5). But in this context, BISM is expected to be very sensitive to the boundary conditions. To illustrate it, we used FEM simulations and compared the BISM calculation of S_{tot} when assuming zero stress at the edge of the cell and when fixing the boundary stress with the surface forces at the edge of the cell: $S_{tot} \cdot \vec{n} = \vec{f}_m$, with \vec{n} the normal to the edge of the cell. Figure 6 shows that setting appropriate boundary conditions brings the BISM curve closer to the FEM curve, even further from the boundary.

SI-3. Relationship between $divS_c/E_c$ and \vec{f}_m for a semi infinite elastic medium covered by a thin elastic film

Cells are modeled as a thin elastic plate firmly bound to the matrix. The matrix itself is modeled as a semi infinite elastic medium (Fig. 7). We note E_c and ν_c the Young's modulus and the Poisson's ratio of the elastic plate of thickness h . E_m and ν_m are the Young's modulus and the Poisson's ratio of the matrix. We analyze the effect of a stress generator localized in the thin elastic plate, with surface force \vec{f}_{act} (Fig. 7). The semi infinite medium resists the active stress with a surface force $-\vec{f}_m$, \vec{f}_m being the stress that is measured by TFM. As the film is firmly bound to the semi infinite medium, the displacement field of the median plane in the film is identical to the displacement

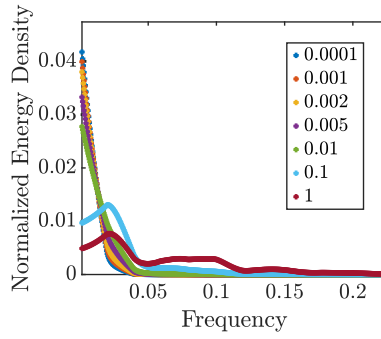


FIG. 5. Increasing the regularization parameter in BISM calculation filters the low frequencies. The colors refer to values of the regularization parameter.

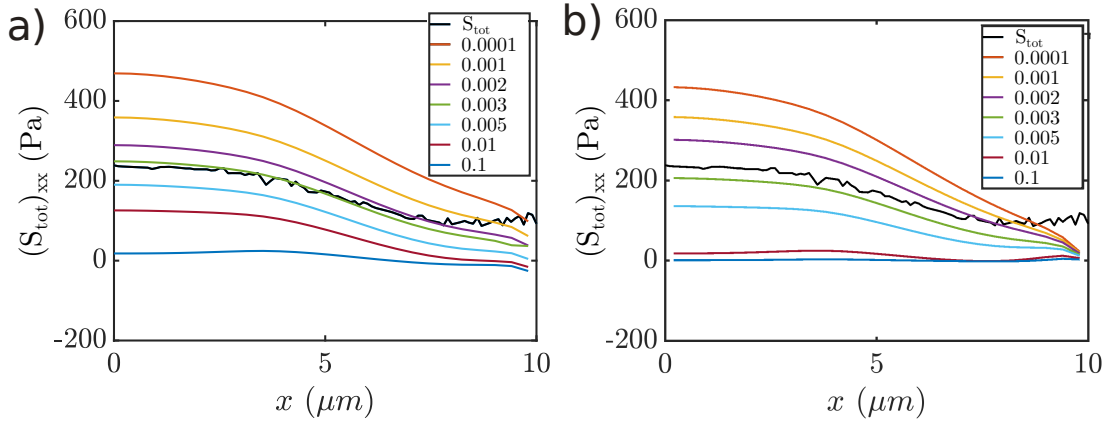


FIG. 6. Effect of boundary conditions on the solution of BISM algorithm for the set-up shown in Fig. 2 of the main text. a) Boundary conditions are given by the surface forces \vec{f}_m at the edge of the cell. b) Zero stress is assumed at the edge of the cell, as in [7]. The FEM calculation is shown in black. The other colors refer to values of the regularization parameter.

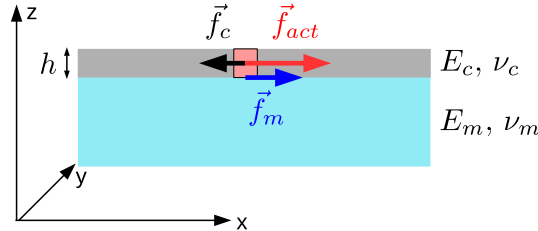


FIG. 7. Elastic model for a cell or a cell colony (in grey) firmly adhered to a semi infinite deformable matrix (in blue). The respective Young's moduli for the thin film and the semi infinite layer are E_c and E_m and their Poisson's ratio ν_c and ν_m . The cell is assumed to bear a point of stress generation, \vec{f}_{act} (red square). The thin film opposes a resistance \vec{f}_c to the active stress, and the matrix opposes $-\vec{f}_m$.

field atop the semi infinite medium. We note it \vec{u} . \vec{u} and \vec{f}_m are therefore linked by the Boussinesq equation [13]. In the Fourier space,

$$\vec{u}_q = G_q \cdot \vec{f}_{mq} \quad (11)$$

where \vec{q} is the wave vector and q denotes Fourier transformation. G_q is the Fourier transform of the Green function solution of Boussinesq's problem. As \vec{f}_{act} is a transverse stress, \vec{u} is also transverse as a consequence of the thin film approximation: $u_z = 0$. G_q thus simply writes [12]:

$$G_q = \frac{2(1 + \nu_m)}{E_m q^3} \begin{pmatrix} (1 - \nu_m)q_x^2 + q_y^2 & -\nu_m q_x q_y \\ -\nu_m q_x q_y & q_x^2 + (1 - \nu_m)q_y^2 \end{pmatrix} \quad (12)$$

and the stress in the thin film has only in plane components independent of z :

$$S_c = \begin{pmatrix} \sigma_{xx} & \sigma_{xy} \\ \sigma_{xy} & \sigma_{yy} \end{pmatrix}$$

$$\text{with } \begin{cases} \sigma_{xx} = \frac{E_c}{1-\nu_c^2} \left(\frac{\partial u_x}{\partial x} + \nu_c \frac{\partial u_y}{\partial y} \right) \\ \sigma_{yy} = \frac{E_c}{1-\nu_c^2} \left(\frac{\partial u_y}{\partial y} + \nu_c \frac{\partial u_x}{\partial x} \right) \\ \sigma_{xy} = \frac{E_c}{2(1+\nu_c)} \left(\frac{\partial u_x}{\partial y} + \frac{\partial u_y}{\partial x} \right) \end{cases} \quad (13)$$

From Eq. (13), $\text{div}S_c$ writes in the Fourier space:

$$(\text{div}S_c)_q = A_q \vec{u}_q \quad (14)$$

with

$$A_q = -\frac{E_c}{2(1-\nu_c^2)} \begin{pmatrix} 2q_x^2 + (1-\nu_c)q_y^2 & (1+\nu_c)q_xq_y \\ (1+\nu_c)q_xq_y & (1-\nu_c)q_x^2 + 2q_y^2 \end{pmatrix} \quad (15)$$

Combination of Eqs (11) and (14) leads to:

$$\begin{aligned} (\text{div}S_c)_q &= A_q G_q \vec{f}_{mq} \\ &= -\frac{E_c(1+\nu_m)}{qE_m(1-\nu_c^2)} \begin{pmatrix} 2(1-\nu_m)q_x^2 + (1-\nu_c)q_y^2 & (1+\nu_c-2\nu_m)q_xq_y \\ (1+\nu_c-2\nu_m)q_xq_y & (1-\nu_c)q_x^2 + 2(1-\nu_m)q_y^2 \end{pmatrix} \vec{f}_{mq} \end{aligned} \quad (16)$$

$\text{div}S_c$ and \vec{f}_m are thus proportional in the Fourier space, meaning that $\text{div}S_c$ and \vec{f}_m are linked by a Green function, H , which Fourier transform is provided by Eq. (16):

$$\text{div}S_c(\vec{r}) = \int H(\vec{r}-\vec{r}') \vec{f}_m(\vec{r}') d\vec{r}' \quad (17)$$

Experimentally, we observe that $\text{div}S_c$ and \vec{f}_m are proportional (Eq. (6) in the main text). This is attained when off-diagonal terms in H are negligible and the diagonal terms in H are close to constant. We compared numerically the x and y components of $(\text{div}S_c)$ for a gaussian stress \vec{f}_m along the x direction. This allowed separating the contributions of the diagonal and the off-diagonal terms in Eq. (16). We obtained that the contribution of the off-diagonal term is negligible compared to the diagonal term (Fig. 8), thus confirming that the off-diagonal terms in H can be neglected. We then addressed the inverse Fourier transform of the diagonal terms of H . To this end, we introduce the cut-off

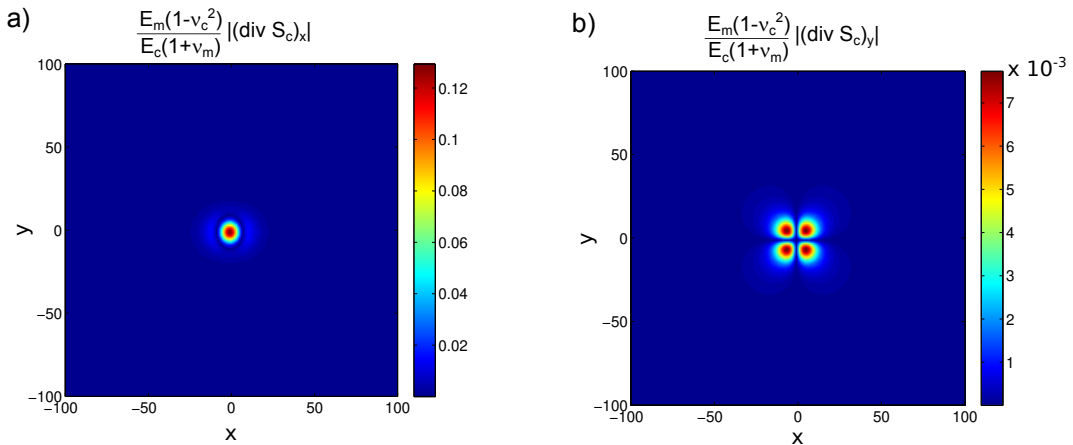


FIG. 8. Amplitudes of a) x and b) y components of $\text{div}S_c$ in response to a gaussian stress \vec{f}_m along the x direction, of standard deviation 5 pixels. The x component comes from the inverse Fourier transform of the diagonal term in the matrix in Eq. (16) while the y component comes from the off-diagonal term. ($\nu_m = 0.5$, $\nu_c = 0.5$)

length a of the sampling. We obtain:

$$H(\vec{r}) \simeq -\frac{E_c(1+\nu_m)}{a^3 E_m(1-\nu_c^2)} \begin{pmatrix} I_1(\frac{r}{a})(2(1-\nu_m)\cos^2\phi + (1-\nu_c)\sin^2\phi) - I_2(\frac{r}{a})\cos 2\phi(1+\nu_c-2\nu_m) & 0 \\ 0 & I_1(\frac{r}{a})((1-\nu_c)\cos^2\phi + 2(1-\nu_m)\sin^2\phi) + I_2(\frac{r}{a})\cos 2\phi(1+\nu_c-2\nu_m) \end{pmatrix} \quad (18)$$

with r and ϕ the radial coordinates of the position \vec{r} . I_1 and I_2 in Eq. (18) are respectively:

$$I_1(x) = \frac{2\pi}{3} {}_1F_2\left(\frac{3}{2}; 1, \frac{5}{2}; -\frac{x^2}{4}\right)$$

$$I_2(x) = 4 \int_0^1 \sqrt{1-u^2} \left(\frac{\sin(ux)}{ux} + 2\frac{\cos(ux)}{u^2x^2} - 2\frac{\sin(ux)}{u^3x^3} \right) du$$

with ${}_1F_2$ the generalized hypergeometric function. As shown on Figure 9, I_1 and I_2 are fast decaying functions,

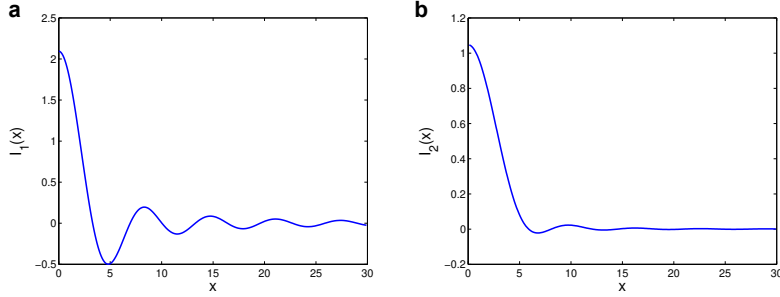


FIG. 9. Plots of I_1 (a) and I_2 (b) in Eq. (18).

and thus both diagonal terms in H are also fast decaying. Then we expect that the relationship between $\text{div}S_c$ and \vec{f}_m shows difference depending whether the extent of the force field is smaller or larger than the sampling size. To confirm it, Eq. (17) was solved for a Gaussian surface force field \vec{f}_m of standard deviation σ smaller or larger than the sampling size a . We obtained that when the width of the Gaussian force field is smaller than the sampling size ($\sigma < a$), the spreading of $\text{div}S_c$ is roughly given by the sampling size (Fig. 10b) and $\text{div}S_c$ and \vec{f}_m correlate linearly with a reasonable precision (Fig. 10c). On the other hand, when the width of the Gaussian force field exceeds the sampling size ($\sigma > a$), $\text{div}S_c$ shows oscillations in consistence with the shape of the Green function H and spreads on a width close to the width of the force field (Fig. 10e). In this case, the linear correlation between $\text{div}S_c$ and \vec{f}_m is lost (Fig. 10f). The experimental observation of a linear correlation between $\text{div}S_c$ and \vec{f}_m (Fig. 3f in the main text) thus leads to the conclusion that the surface forces that are transmitted to the substrate apply on areas that are smaller than the experimental sampling size. It also leads to the conclusion that this linear correlation is approximate and is related to the narrow extent of the surface forces relative to the sampling size.

From this conclusion, we can evaluate the slope of the linear correlation by solving Eq. (17) for a Dirac force. We obtain:

$$\text{div}S_c \simeq -\frac{\pi E_c(1+\nu_m)}{3a E_m(1-\nu_c^2)}(3-2\nu_m-\nu_c)\vec{f}_m \quad (19)$$

The experimental length h_0 then directly relates to the sampling size a .

$$h_0 \simeq a \frac{3(1-\nu_c^2)}{\pi(1+\nu_m)(3-2\nu_m-\nu_c)} \quad (20)$$

SI-4. Sensitivity of the linear relationship with sampling and filtering

Experimentally, we observed that $\text{div}S_c$ and \vec{f}_m correlate linearly. We investigate here how this linear relationship is sensitive to the spatial sampling and to the filtering of the cell-to-matrix stress field that is commonly performed to limit noise effects.

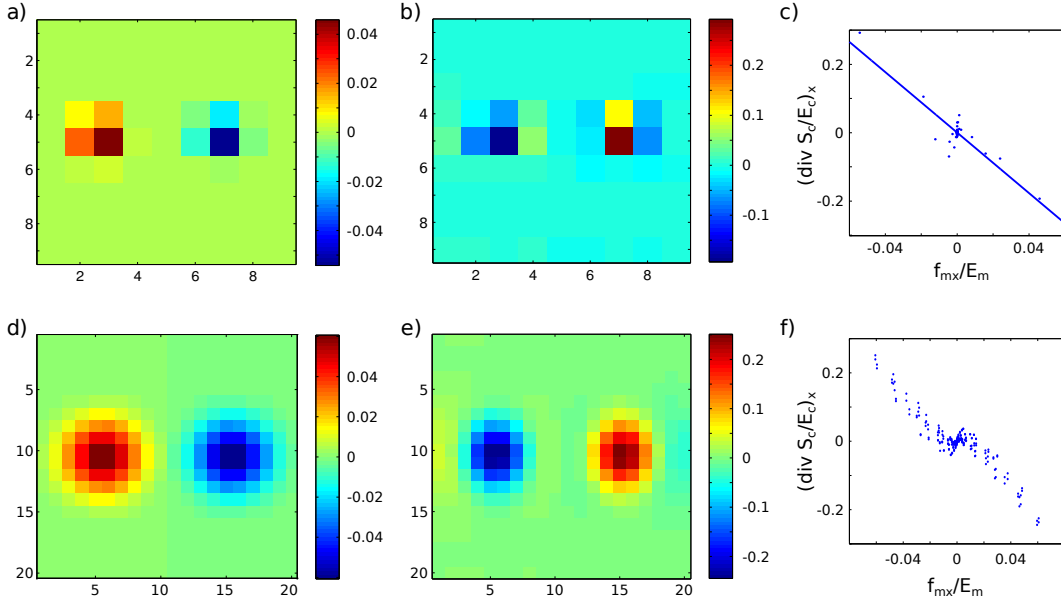


FIG. 10. Amplitude of $(\text{div} S_c)_x$ in response to a stress dipole \vec{f}_m . The dipole consists in opposite Gaussian fields of standard deviation σ along the x -direction. As in experiments, $\text{div} S_c$ and \vec{f}_m are sampled on a grid of size a . This is done numerically using the function *imresize* from MatlabTM. a) Spatial distribution of the x -component of \vec{f}_m for $\sigma = 2$ and $a = 7$. b) Associated spatial distribution of the x -component of $\text{div} S_c$. c) $\text{div} S_c$ and \vec{f}_m correlate linearly (slope -4.4 , $r^2 = 0.81$). d-f) Same as a-c) with a Gaussian stress field of width $\sigma = 6$ and a sampling size $a = 3$. $\text{div} S_c$ and \vec{f}_m do not show a linear correlation. The kink near 0 comes from the oscillations of the Green function H .

We first analyzed how sampling would impact this relationship. The Shannon criterion provides an optimal sampling size of 3 pixels, meaning that the pixel size of the stress fields is 3 times larger than the pixel size of the original images. We varied the pixel size of the stress fields from 1 to 64 pixels. As shown on Fig. 11, we obtained that the linear relationship still holds but the slope of the line varies with the sampling. This thus shows that the relationship between $\text{div} S_c$ and \vec{f}_m is intrinsically linear, but the slope of the line results from the numerical treatment.

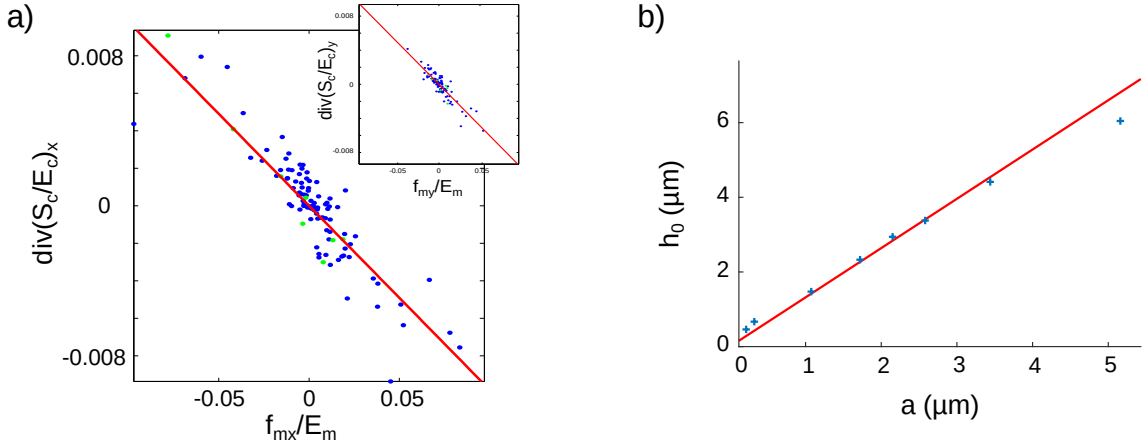


FIG. 11. a) Under-sampling the stress fields does not alter the linear correlation between $\text{div} S_c$ and \vec{f}_m . Pixel size of the stress fields: 64 pixels. Green dots stand for paxillin positive pixels. The red line is the fit (correlation coefficients: 0.93 for the x -component, 0.96 for the y -component). b) The slope of the linear correlation, $-1/h_0$, is sensitive to the sampling of the stress fields.

Secondly, we tested how filtering of the cell-to-matrix stress field influences the shape of this relationship. Filtering is often used in TFM algorithms to smooth the signal and limit noise effects. While smoothing the displacement field by application of a wiener filter did not significantly affect the shape nor the slope of the curve (wiener2 function in Matlab, not shown), we observed that a too strong filtering of the cell-to-matrix stresses \vec{f}_m disrupts the linear

correlation between $divS_c$ and \vec{f}_m (Fig. 12). To show it, the cell-to matrix stress field was filtered with a low-pass filter that removed the high frequencies components (Fig. 12).

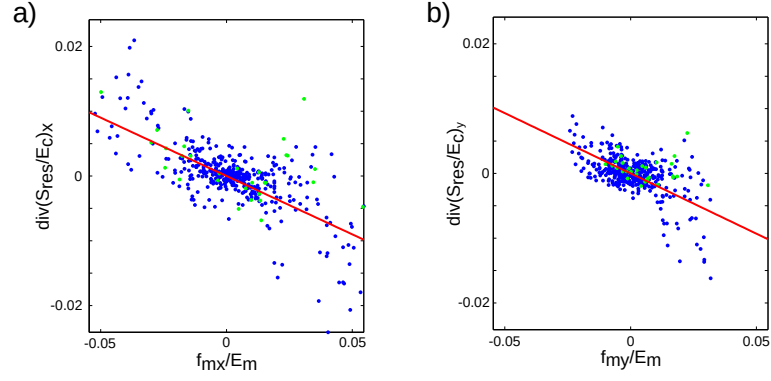


FIG. 12. Filtering of the cell-to-matrix stress field may hide the linear correlation between $divS_c$ and \vec{f}_m . x (a) and y (b) components are shown. Stress components from wave vectors with amplitude larger than $q_{max}/6$, with q_{max} the maximal amplitude of the wave vector were removed. Green dots stand for paxillin positive pixels. The red line is an attempt of linear fit. The correlation coefficient is of order of 0.6.

SUPPLEMENTARY FIGURES

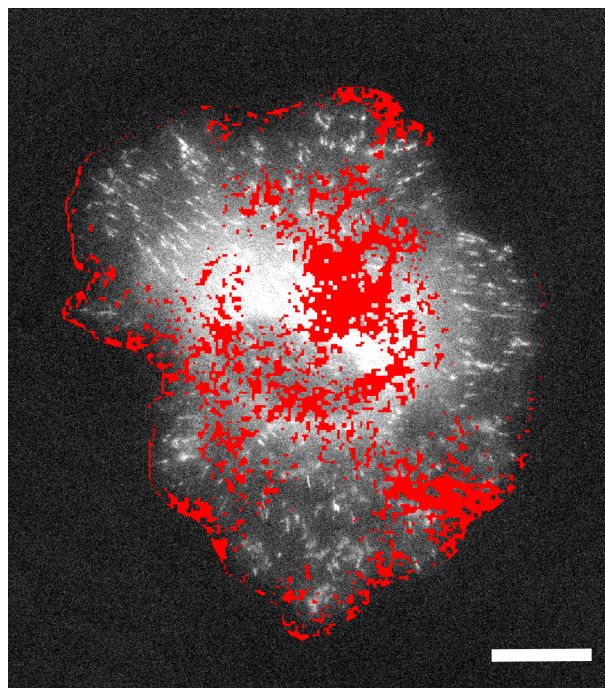


FIG. 13. REF52 cells transmit surface forces to the extracellular matrix also out of focal adhesions. Focal adhesions are stained with YFP-paxillin. Red pixels show places where the surface forces \vec{f}_m have an amplitude below the 0.95 percentile of the noise level.

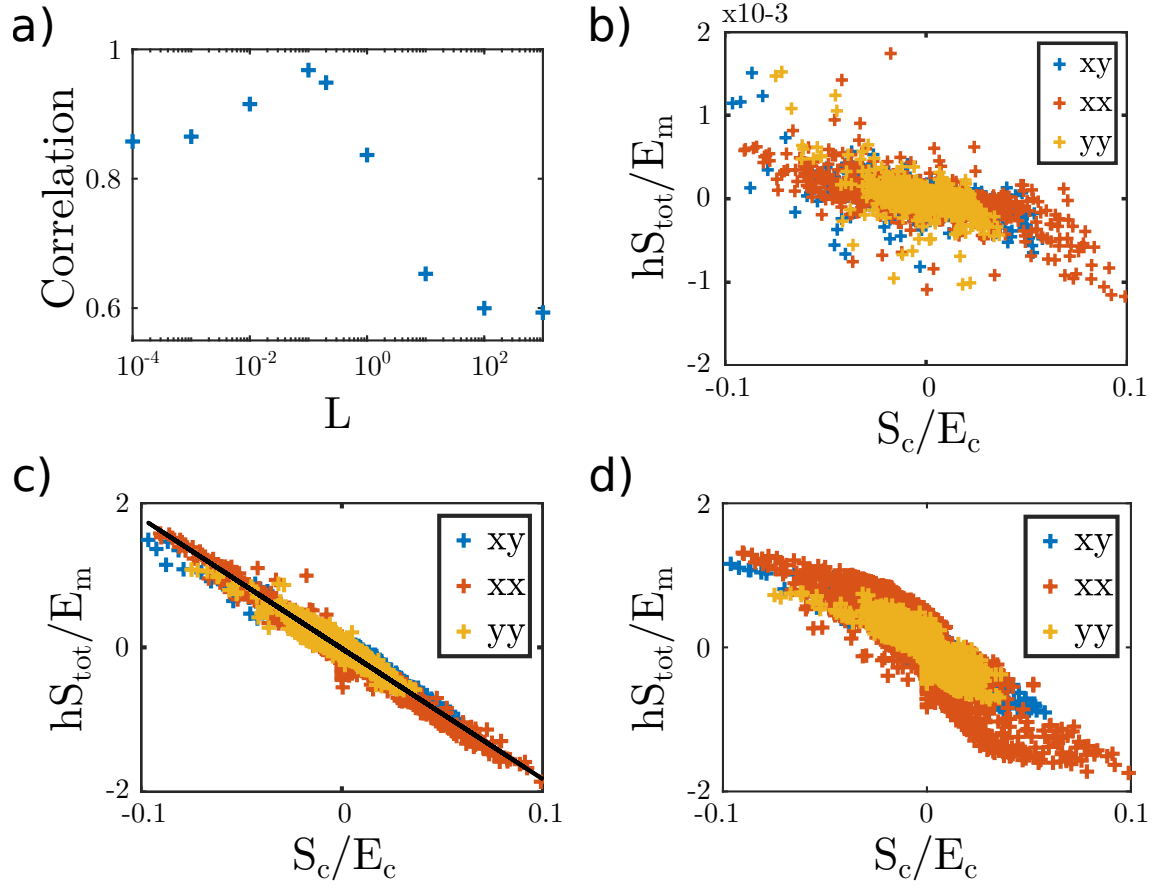


FIG. 14. Shape of the relationship between S_{tot} and S_c for different values of the regularization parameter L for the single cell of Fig. 3a in the main text. a) Correlation between BISM and ISM calculation as a function of the regularization parameter L . b) $L = 10^{-4}$ (under regularization). c) $L = 0.1$. This value corresponds to the maximal correlation between both quantities. It is close to the one that the discrepancy principle selects ($L = 0.06$). d) $L = 800$ (over regularization).

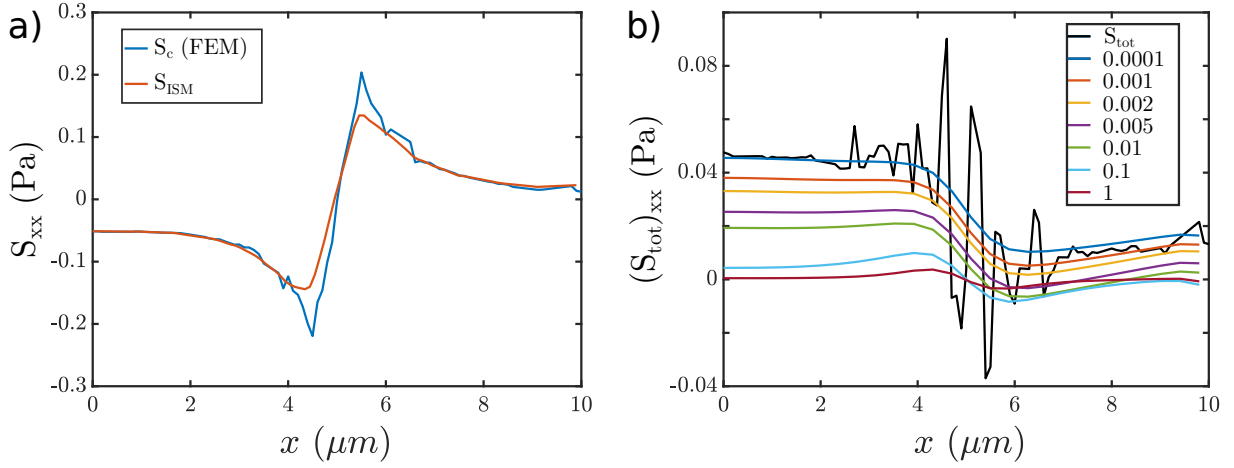


FIG. 15. Comparison of a) S_{ISM} and b) S_{BISM} with S_c and S_{tot} calculated with FEM simulations for a uniformly adhered plate submitted to a local force field \vec{f}_{act} with gaussian distribution with similar design as in Fig. 2 of the main text. Here the size of the region with force generation is small compared to the size of the plate (force patch of $1\mu m$, $\sigma = 0.25\mu m$). ISM and BISM well account for the values of S_c (blue line) and S_{tot} (black line). Influence of the value of regularization parameter on the shape of S_{BISM} is shown in (b) (values are listed in the legend).

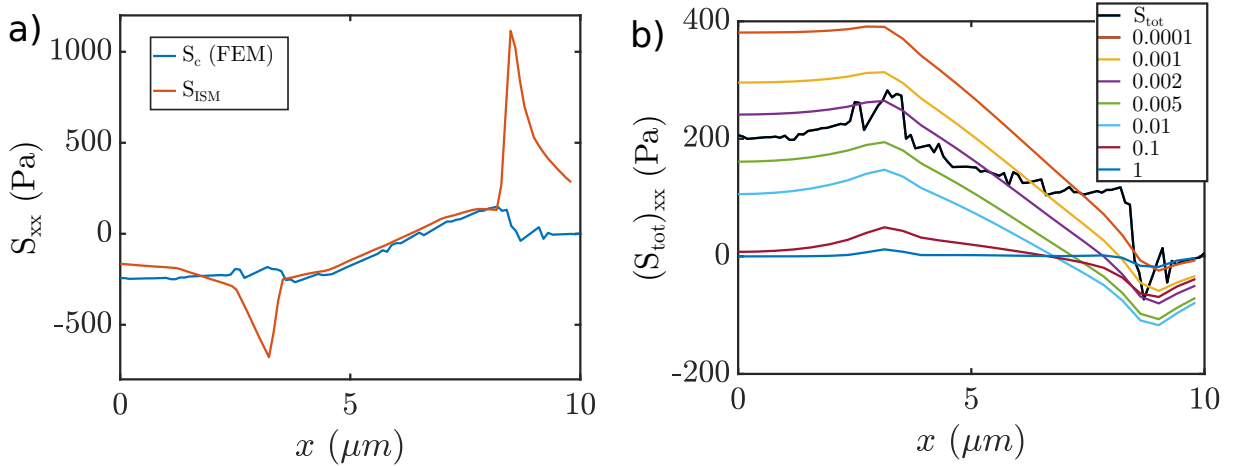


FIG. 16. Comparison of a) S_{ISM} and b) S_{BISM} with S_c and S_{tot} calculated with FEM simulations for a plate only adhered in the patches where active surface forces apply. The characteristics of the active force field is identical to Fig. 2 in the main text (force patch of $5\mu m$, $\sigma = 2\mu m$). Here ISM is no more relevant out of the adhered patch and BISM also fails to represent S_{tot} (shown with a black line). Influence of the value of the regularization parameter on the shape of S_{BISM} is shown in (b) (values are listed in the legend).

* helene.delanoe-ayari@univ-lyon1.fr

† alice.nicolas@cea.fr

- [1] A. Barbacci, J. Diener, P. Héémon, B. Adam, N. Donès, L. Reveret, and B. Moulia, A robust videogrametric method for the velocimetry of wind-induced motion in trees., *Agric. For. Meteorol.*, 220 (2014).
- [2] B. D. Lucas and T. Kanade, An iterative image registration technique with an application to stereo vision., in *Int. Joint Conf. on Artificial Intelligence* (1981) pp. 674

- [3] C. N. Holenstein, U. Silvan, and J. G. Snedeker, High-resolution traction force microscopy on small focal adhesions - improved accuracy through optimal marker distribution and optical flow tracking., *Sci. Rep.* **7**, 41633 (2017).
- [4] J. Y. Bouguet, *Pyramidal implementation of the Lucas Kanade feature tracker description of the algorithm.*, Tech. Rep. (Intel Corporation, Microprocessor Research Labs, 2000).
- [5] J. P. Butler, I. M. Tolic-Nørrelykke, B. Fabry, and J. J. Fredberg, Traction fields, moments, and strain energy

- that cells exert on their surroundings., *Am. J. Physiol. Cell Physiol.* **282**, C595 (2002).
- [6] M. Moussus, C. der Loughian, D. Fuard, M. Courçon, D. Gulino-Debrac, H. Delanoë-Ayari, and A. Nicolas, Intracellular stresses in patterned cell assemblies, *Soft Matter* **10**, 2414 (2014).
- [7] V. Nier, S. Jain, C. T. Lim, S. Ishihara, B. Ladoux, and P. Marcq, Inference of internal stress in a cell monolayer., *Biophys. J.* **110**, 1625 (2016).
- [8] U. S. Schwarz, N. Q. Balaban, D. Riveline, A. Bershadsky, B. Geiger, and S. A. Safran, Calculation of forces at focal adhesions from elastic substrate data: the effect of localized force and the need for regularization., *Biophys. J.* **83**, 1380 (2002).
- [9] A. Caboussat and R. Glowinski, Regularization methods for the numerical solution of the divergence equation $\nabla \cdot u = f$, *J Comput Math*, 354 (2012).
- [10] M. Dembo, T. Oliver, A. Ishihara, and K. Jacobson, Imaging the traction stresses exerted by locomoting cells with the elastic substratum method., *Biophys. J.* **70**, 2008 (1996).
- [11] D. Ambrosi, Cellular traction as an inverse problem, *SIAM J. Appl. Math.* **66**, 2049 (2006).
- [12] B. Sabass, M. L. Gardel, C. M. Waterman, and U. S. Schwarz, High resolution traction force microscopy based on experimental and computational advances, *Biophys. J.* **94**, 207 (2008).
- [13] L. Landau and E. Lifchitz, *Theory of elasticity* (Mir Ed., 1967).